

Microstructural Evolution and Mechanical Properties of CSEF/M P92 Steel Weldments Welded Using Different Filler Compositions



NITIN SAINI, MANAS MOHAN MAHAPATRA, and RAHUL S. MULIK

In the present investigation, P92 steel weld joints were prepared using a shielded metal arc welding (SMAW) process for two different fillers, E911 and P92. A comparative study was performed on the microstructural evolution, tensile strength, microhardness, and Charpy toughness across the P92 steel weldments in the as-welded and post-weld heat-treated (PWHT) conditions. The PWHT was performed at 760 °C for 2 hours. To study the effect of the different filler metals and PWHT on the mechanical properties, longitudinal and transverse tensile tests were carried out at room temperature for a constant cross-head speed of 1 mm/min. In the longitudinal direction, the tensile strength of the P92 steel welds was measured as 958 ± 35 and 1359 ± 38 MPa for the E911 and P92 filler, respectively. In the as-welded condition, the transverse tensile specimens were fractured from the fine-grained heat-affected zone or inter-critical heat-affected zone (FGHAZ/ICHAZ) and, after PWHT, the fracture location was shifted to over-tempered base metal from the FGHAZ/ICHAZ. After the PWHT, the tempering reaction resulted in lowering of the hardness throughout the weldment. After PWHT, the Charpy toughness of the weld fusion zone and heat-affected zone (HAZ) of the E911 filler weldments was measured as 66 ± 5 and 142 ± 8 J, respectively. The minimum required Charpy toughness of 47 J (EN1557: 1997) was achieved after the PWHT for both E911 and P92 filler.

<https://doi.org/10.1007/s11661-018-4797-7>

© The Minerals, Metals & Materials Society and ASM International 2018

I. INTRODUCTION

IN recent years, to enhance the efficiency of steam power plants for economic and environmental reasons, the need for creep strength-enhanced ferritic/martensitic (CSEF/M) steels has increased.^[1,2] The simplest way to achieve higher efficiency is to increase the inlet pressure and temperature of the steam that passes through the turbines.^[3] The primary candidate material for the construction of supercritical coal-fired boilers in the power industries is CSEF/M steels (mainly P91 and P92 steels).^[4] The CSEF/M steels offer high creep resistance, excellent thermal conductivity, good toughness, ductility, a low coefficient of thermal expansion, high resistance to stress corrosion cracking and oxidation.^[5–7] Microstructural stability at elevated temperatures and good weldability are also lucrative properties exhibited

by CSEF/M steels.^[8,9] The application of low chromium ferritic alloys [2–3 pct chromium (Cr)] is limited in the boiler up to service temperatures of 500–550 °C due to environmental degradation from the fire side.^[10] Ferritic steels in the range of 9–12 pct Cr, such as T91, T92, and E911, appear to be capable of being used up to a temperature of 650 °C.^[11,12]

In P92 steel, the primary alloying element is Cr which improves the oxidation and corrosion resistance. The other alloying elements are tungsten (W), vanadium (V), manganese (Mn), molybdenum (Mo), silicon (Si), niobium (Nb), carbon (C), and small amount of boron (B) (up to 0.005 pct).^[13] These alloying elements integratively improve the properties at elevated temperature. The P92 steel offers enhanced creep strength that results from the combination of precipitation and solid solution hardening.^[14] It also offers better creep strength as compared to any other CSEF/M steels by forming $M_{23}(C, B)_6$ that reduce the coarsening rate of coarse carbide particles.^[15]

Study of the welded joint behavior is critically important as most of the failures in boiler tubes occur in the weld joints only.^[16,17] To increase the range of applications of T/P92 base material, the development of compatible consumables is mandatory. But exceptionally a slightly higher Mn (~ 0.7 pct) and a deliberate Ni addition (~ 0.5 pct) have been advisable to achieve a

NITIN SAINI and RAHUL S. MULIK are with the Department of Mechanical and Industrial Engineering, Indian Institute of Technology Roorkee, Roorkee, Uttarakhand, 247667, India. Contact e-mail: nit030078@gmail.com MANAS MOHAN MAHAPATRA is with the School of Mechanical Sciences, Indian Institute of Technology, Bhubaneswar, Odisha, 751013, India.

Manuscript submitted November 21, 2017.

Article published online July 5, 2018

satisfactory weld metal strength and Charpy toughness.^[18,19] Welding introduces localized changes in the microstructure, which become the life-limiting factor for these steels. In particular, type IV cracking is a phenomenon in which an enhanced rate of creep void formation occurs in the fine-grained heat-affected zone (FGHAZ) or inter-critical heat-affected zone (ICHAZ).^[20] During welding of P92 steel, the temper martensitic microstructure is adversely altered by the formation of fresh martensite in the weldments (weld fusion zone + heat-affected zones).^[21] The nominal strength of P92 steel may be compromised by susceptibility to type-IV cracking in HAZs of welds while increasing contents of ferrite-forming elements like V, Nb, W, Mo, and Cr, may lead to excessive formation of δ -ferrite.^[22] Due to type IV cracking, the premature failure in the cross-welds is observed at an earlier stage of creep exposure as compared to the base materials. The type IV cracking also reduces the creep rupture strength of cross-welds by 50 pct as compared to base materials.^[23] The presence of δ -ferrite patches in P92 steel welds has been observed a negative effect on mechanical properties due to notch sensitivity of the δ -ferrite.^[24–26]

The post-weld heat treatment (PWHT) is a mandatory operation carried to reduce the non-equilibrium microstructure gradient and minimize the hardness mismatch across the weldment.^[27–29] The specification of preheating and PWHT conditions is an important concern because P92 steel is a high-strength alloy steel that normally transforms completely to martensite during air cooling.^[30] To reduce the hardness and improve the ductility of the weld/HAZ, the PWHT is carried out just after welding at 760 °C (± 10 °C) for the P92 steel.^[31] The PWHT resulted in a greater reduction in hardness, improved ductility and toughness of the weldments.^[32]

II. MATERIAL AND EXPERIMENTAL DETAILS

The normalized and tempered P92 steel plates were received from Bharat Heavy Electronics Limited (BHEL) Haridwar, India. As per the supplier, P92 steel plates were normalized at 1000 °C for 1 hour and air-cooled and tempered at 760 °C for 2 hour, followed by air cooling.^[15] The chemical composition of P92 steel was analyzed using an optical emission spectrometer. The 4-mm-diameter flux-coated E911 consumable filler rod was received from BHEL Haridwar, India and the 4-mm-diameter flux-coated P92 filler rods were received from the Mailam India Limited, Pondicherry, India.

The chemical compositions of P92 steel, fillers (E911 and P92), and welds are depicted in Table I.

The plates of size 150 mm \times 60 mm \times 12 mm were machined for the weld joints from the as-received P92 steel plate. A conventional V-groove design was prepared for making the weld joint with a groove angle and root height of 37.5 deg and 1.5 mm, respectively, as shown in Figure 1(a). The welding process parameters for the root and filler pass are given in Table II. Shielded metal arc welding (SMAW) was carried out to prepare the P92 steel weld joints using 4-mm-diameter flux-coated E911 and P92 fillers. Before welding, the preheating of plates was performed in the range of 280–300 °C. The complete weld joints of P92 steel are shown in Figure 1(c). After welding, the first plate was allowed to cool in the air up to room temperature. To find the influence of post-weld heat treatment (PWHT) on the weld and HAZ microstructure, after welding plates were subjected to post-weld heating at 250 °C for 40 minutes and then air cooling up to 100 °C^[33] and followed by PWHT at 760 °C for 2 h and then air-cooled up to room temperature (Figure 2). The inter-pass temperature during welding was maintained in the range of 250 to 300 °C.

To determine the tensile properties of the P92 steel weldments, longitudinal and transverse tensile specimens were prepared as per ASTM E8/E8M.^[34] The schematic shows the location and dimensions of the Charpy toughness and tensile test specimens removed from the welded plates, as shown in Figure 3. The gauge length and width of the transverse tensile specimens were taken as 25 and 6 mm, respectively. For longitudinal specimens, the width and gauge length were taken as 10 and 15 mm, respectively. To characterize the microstructure of P92 steel weldments, the specimens were polished up to 2000 grit size silicon carbide (SiC) emery papers and etched with Vilella's solution (1 g picric acid + 5 mL hydrochloric acid + 100 mL ethanol). The microstructural analysis of various zones of the P92 weldments was performed using the optical microscope (OM) and field-emission scanning electron microscope (FESEM). To determine the Charpy toughness of P92 steel weld fusion zone and heat-affected zone (HAZ), standard size V-notch samples were prepared with dimensions of 55 mm \times 10 mm \times 10 mm according to ASTM A370.^[35] The microhardness of as-received and welded specimens was measured using Vickers Hardness Tester (Omnitech-S. Auto), at the load of 500 g and dwell time of 10 seconds. To study the fracture surface morphology of tensile tested specimens, FESEM was utilized.

Table I. Composition of the P92 Steel and Different Fillers (Weight Percent)

Element	C	Mn	P	S	Si	Cr	Mo	V	Al	Nb	W	Cu	Ni	N	Fe
P92 steel	0.10	0.58	0.007	0.003	0.48	9.09	0.42	0.24	0.02	0.07	1.86	0.03	0.30	0.02	rest
E911 filler	0.11	0.80	0.010	0.008	0.25	9.50	1.00	—	—	0.05	1.0	—	0.50	0.05	rest
P92 filler	0.11	0.61	0.008	0.005	0.19	8.90	1.01	0.22	—	0.06	1.82	0.04	0.66	0.06	rest
Weld using E911 filler	0.11	0.75	0.008	0.005	0.34	9.30	0.84	0.08	—	0.05	1.2	0.03	0.45	0.04	rest
Weld using P92 filler	0.13	0.71	0.007	0.005	0.30	9.04	0.97	0.23	—	0.06	1.75	0.04	0.51	0.05	rest

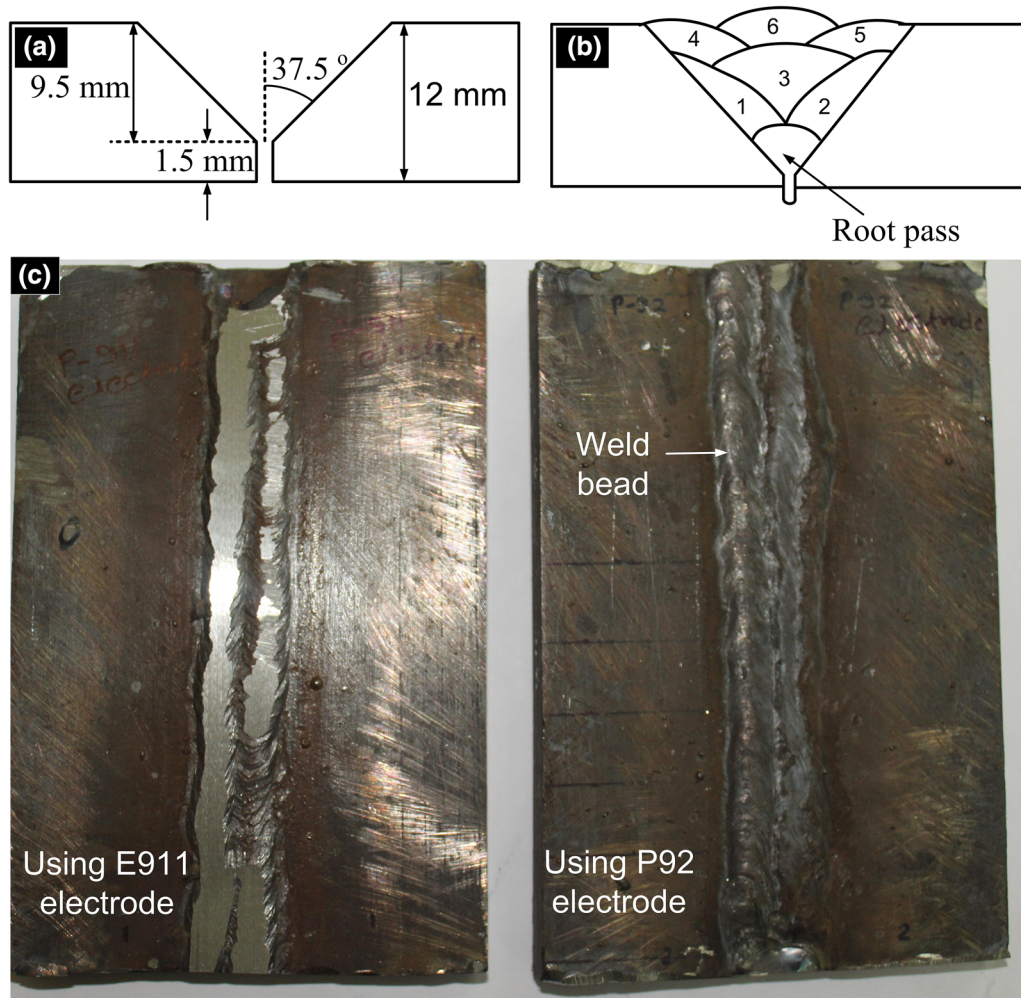


Fig. 1—(a) Schematic of groove design, (b) schematic of the weld passes, and (c) complete weld joints.

Table II. Welding Process Parameters for Root Pass and Filler Pass

Passes	Process	Current (I) Amps	Voltage (V) Volts	Travel Speed (T) (mm/min)	Arc Efficiency	Avg. Heat Input (kJ/mm)
Root pass	GTAW	115-120	14-15	130	0.75	0.079
Filler pass 1	SMAW	140	22-23	150	0.75	0.126
Filler pass 2	SMAW	140	21-23	145	0.75	0.127
Filler pass 3	SMAW	140	22-24	148	0.75	0.130
Filler pass 4	SMAW	140	21-24	140	0.75	0.135
Filler pass 5	SMAW	140	23-25	145	0.75	0.139
Filler pass 6	SMAW	140	22-26	140	0.75	0.144

III. RESULTS AND DISCUSSION

A. Microstructure and Mechanical Properties of As-Received P92 Steel

Secondary electron micrograph and optical micrograph of as-received P92 steel is shown in Figures 4(a) and (b), respectively. The microstructure of as-received P92 steel consists of distinct prior austenite grain boundaries (PAGBs), tempered equiaxed laths, lath packets, lath boundaries, and lath blocks. The precipitates located along the boundaries and lath packets are

confirmed as Cr, Fe, and Mo-rich $M_{23}C_6$ carbide precipitates, while spherical fine precipitates are confirmed as V and Nb-rich MX-type precipitates.^[36,37] The alloying elements such as C, Cr, Mo, V, Fe, and Nb promote the formation of precipitates like Cr-rich $M_{23}C_6$ -type precipitates [M:Cr, Mo, W and Fe] and Nb or V-rich MX-type precipitates [M:V, N and X:C, N].^[38] The spherical MX-type precipitates were observed inside the intra-lath region.^[39] These fine MX-type precipitates enhance the creep strength by impeding the movement of mobile dislocations and

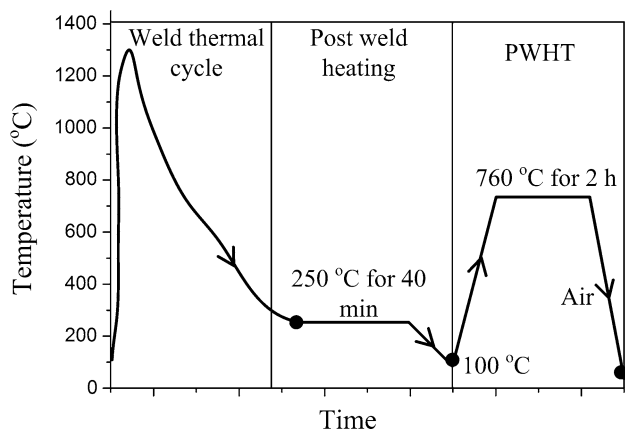


Fig. 2—Schematic of the welding thermal cycle, post-weld heating, and PWHT.

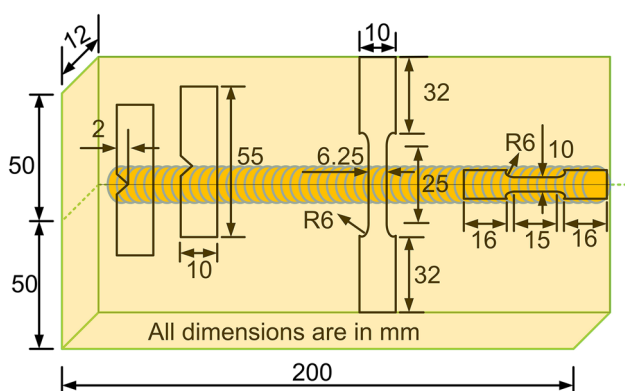


Fig. 3—Schematic of the welded plate showing locations and dimensions of Charpy toughness and tensile test specimens.

sub-grain boundaries, prevent the fine-grained structure from recrystallizing, and provide the precipitation hardening.^[40] The decoration of the precipitates along the martensite lath direction is also observed from Figure 4(a). The optical micrograph of P92 steel shows the tempered martensitic microstructure that consists of PAGBs and precipitates in black dotted form, as shown in Figure 4(b). X-ray diffraction analysis also confirms the presence of $M_{23}C_6$ and MX precipitates in as-received P92 steel, as shown in Figure 4(c). The other precipitates that were observed are as follows: Cr-rich Cr_2N , Fe-rich M_2C , and Cr-rich M_7C_3 . The ultimate tensile strength (UTS), percent elongation, microhardness, and Charpy impact toughness of as-received P92 steel were measured 678 ± 10 MPa, 23 ± 2 pct, 227 ± 4 HV, and 198 ± 8 J, respectively.

B. Microstructure Evolution in As-Welded Condition

Figure 5 shows the basic influence of the weld thermal cycle on the microstructural evolution in the weld fusion zone, heat-affected zones (HAZs), and the related equilibrium phase diagram of P92 steel. For the sake of simplicity, the secondary phase precipitation

reactions have been omitted in the phase diagram. The mechanical properties of the P92 weldments were strongly influenced by the phase transformations occurring within the weldments of P92 steel. The optimized base material properties and microstructure were changed completely during the weld thermal cycle. Under controlled heating and cooling conditions, the relevant phase transformation temperatures of P92 base material are typically considered as re-austenitization temperature (Ac_1) = 835 to 845 °C and upper transformation temperature (Ac_3) = 920 to 930 °C.^[41] At 1.5 pct Ni + Mn content, the Ac_1 temperature was about 790 °C.^[41] Beyond this level, Ac_1 temperature reduced as Ni + Mn content increased. Based on the Ac_1 and Ac_3 temperatures, the various sub-zones formed in P92 steel weldments are discussed below:

1. Weld fusion zone [$T_P > \text{melting temperature } (T_M)$]

In P92 steel, according to the equilibrium phase diagram, austenite (γ) transformed to delta ferrite (δ) at melting temperature. The lower solubility of carbon (C) and other austenite stabilizing elements in ferrite resulted in the escape of these elements out of the δ -ferrite into the remaining austenite regions. Therefore, segregated regions differ locally in chemical composition. The austenite to martensite transformation on cooling can be incomplete, which results in the formation of retained δ -ferrite in the weld fusion zone. In P92 steel, the presence of ferrite stabilizer elements like W, Mo, V, and Nb also promotes the formation of δ -ferrite in the weld fusion zone. Figure 5 shows the δ -ferrite patches in the microstructure of weld fusion zone. Weld zone shows typical untempered columnar laths with a higher weight percentage of carbon (C) and nitrogen (N). The higher weight percentage of C and N in solution matrix results in poor Charpy toughness and high strength of the weld fusion zone.^[42] The lath martensite direction inside the lath packets is also represented in weld fusion zone.

2. Coarse-grained heat-affected zone (CGHAZ) ($T_P \gg Ac_3$)

The zone adjacent to the weld fusion zone (*i.e.*, CGHAZ) experienced temperatures much above the transformation temperature (Ac_3). At such high temperature, almost all precipitates are dissolved, except for some fine NbX-type precipitates that resulted in the formation of the coarse austenite grains.^[43] After cooling, austenite get transformed to the martensite. The dissolution of precipitates resulted in the higher weight percentage of C and N in the solid solution matrix. That leads to poor Charpy toughness and high hardness of CGHAZ among all HAZs. The PAGBs, lath packets and lath directions are also shown in CGHAZ.

3. Fine-grained heat-affected zone (FGHAZ) ($T_P > Ac_3$)

The zone adjacent to CGHAZ (*i.e.*, FGHAZ) experienced the temperatures just above the Ac_3 , which resulted in the formation of small grains of austenite. In

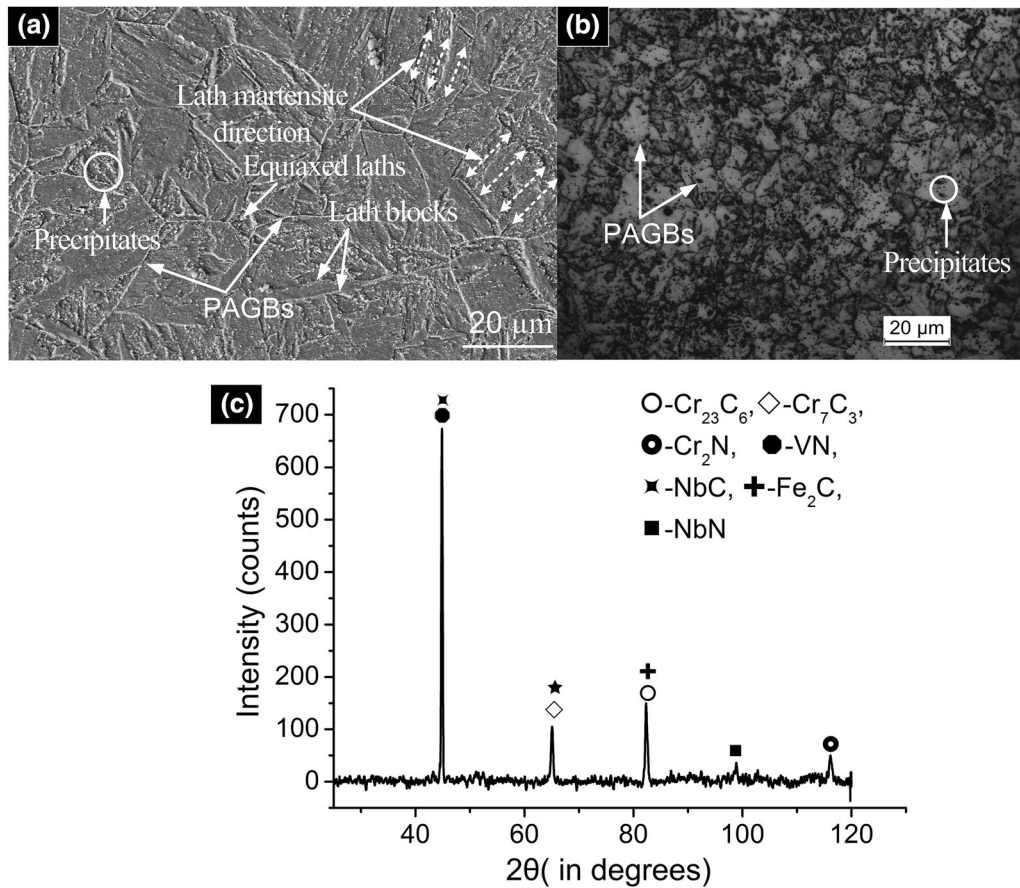


Fig. 4—(a) Secondary electron micrograph of P92 steel in as-received condition, (b) optical micrograph of as-received P92 steel, and (c) x-ray diffraction analysis.

FGHAZ, peak temperature was not too high to dissolve the precipitates completely, thus grain growth limited by the pinning austenite grain boundaries. On cooling, the fine-grained martensitic structure was achieved in the FGHAZ of the weldment. The coarse undissolved $M_{23}C_6$ precipitates are observed clearly in the FGHAZ, as shown in Figure 5. The fine MX precipitates remain undissolved completely. The presence of coarse undissolved $M_{23}C_6$ precipitates and untempered martensite makes the FGHAZ more complex than the CGHAZ.

4. Inter-critical heat-affected zone (ICHAZ) ($Ac_1 < T_P < Ac_3$)

The next zone formed adjacent to the FGHAZ was the ICHAZ, which experienced the peak temperatures between the transformation temperatures Ac_1 and Ac_3 . In this temperature range, the partial transformation of ferrite into austenite occurred during heating, whereas new austenite grains nucleated at prior austenite grain boundaries and the untransformed tempered martensitic microstructure was tempered for a second time by this weld thermal cycle. On cooling, both newly formed martensite and tempered original martensite microstructure were obtained. Partial dissolution of precipitates was noticed in the ICHAZ. The ICHAZ was characterized with the small grain size and the combination of partially tempered and untempered martensite structure.

The lowest hardness and higher Charpy toughness were measured for ICHAZ.^[42]

5. Over-tempered base material ($T_P < Ac_1$)

The zone adjacent to ICHAZ (*i.e.*, over-tempered base material) experienced temperatures below the Ac_1 . Below Ac_1 temperature, the microstructure does not undergo any phase transformation. But the microstructure was locally tempered at higher temperatures as compared to tempering temperature of the base material which might be enhanced the coarsening of precipitates. The zone of unaffected base material experienced the peak temperature below 700 °C at which no visible changes in the microstructure of base material were noticed.^[44]

The micrograph of the weld fusion zone of the P92 steel for E911 filler is shown in Figure 6(a). The weld fusion zone in as-welded state consisted of columnar lath martensitic structure with different martensite lath directions. The weld fusion zone in the as-welded state consisted of a columnar lath martensitic structure with different martensite lath directions. In the FGHAZ, the tempered martensite of the base metal transformed to austenite during the weld thermal cycle. Some undissolved precipitates were also observed in the FGHAZ, as shown in Figures 6(b) and (d). These undissolved precipitates obstruct the growth of austenite grains by

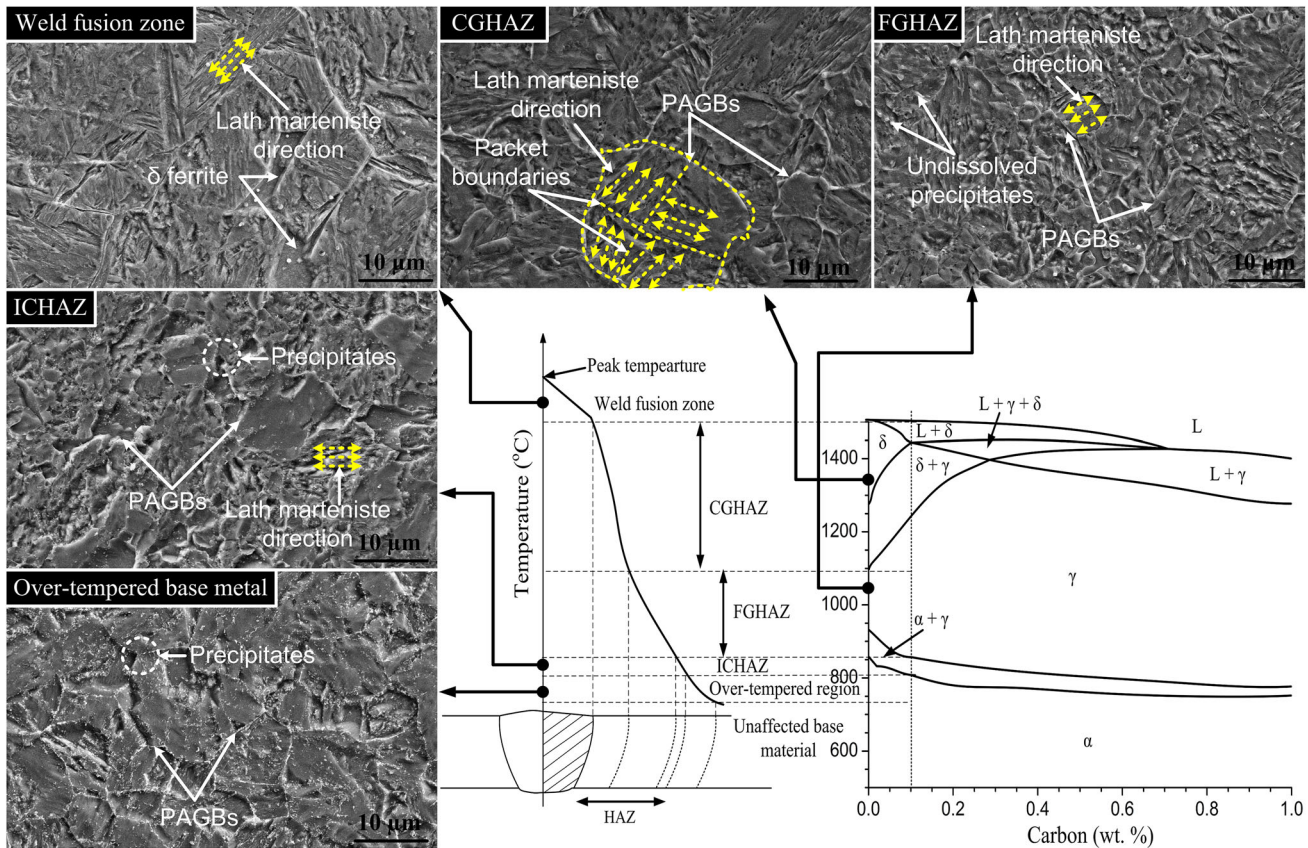


Fig. 5—Schematic of the subzones of the HAZ and their microstructure related to the equilibrium phase diagram of P92 steel weld.

pinning them, which resulted in fine grains of austenite in the FGHAZ. In the FGHAZ of the P92 steel, the lath martensite was formed within the PAGBs with a low length-to-width ratio. In P92 steel, the Schneider formula is utilized to predict the tendency of the δ -ferrite formation. The Schneider formula is given by Onoro^[24] as the ferrite factor (FF), which is the difference of Cr_{eq} and Ni_{eq} [$Ni_{eq} = Ni + 0.5Mn + 30C + 25N + 0.3Cu$] and [$Cr_{eq} = Cr + 2Si + 5V + 1.5Mo + 1.75Nb + 0.75W$]. If $FF \geq 8.5$, the weld shows a high tendency to δ -ferrite formation. Onoro *et al.* reported that a complete absence of δ -ferrite was found in the weld fusion zone with low FF.^[24] In the case of multi-pass welding, the complete transformation of δ -ferrite to austenite occurs due to the additional time for diffusion.^[45] The FF was calculated from weld compositions (Table I) for E911 and P92 filler as 6.5 and 6.2, respectively. In spite of the low value of FF, some δ -ferrite patches were noticed in the weld fusion zone of P92 steel weldments as a result of higher weight percentage of the ferrite stabilizer in the filler metal. Although multi-pass welding and FF is near to limited value for the δ -ferrite evolution, the presence of δ -ferrite was confirmed in the weld fusion zone of P92 steel weldments welded with P92 filler, as shown in Figure 6(c). The distribution of δ -ferrite patches was clearly observed in several local areas of the microstructure, which might have been due to the higher weight percentage of ferrite stabilizers

like W, Mo, V, and Nb in the P92 weld fusion zone as compared to E911 filler weld fusion zone, as given in Table I.

C. Microstructure Evolution of Weldments After PWHT

In the P92 steel, post-weld heat treatment (PWHT) resulted in a coarsening of the existing precipitates as well as nucleation of new precipitates along the PAGBs and lath blocks and also inside the intra-lath region. PWHT of the P92 steel welds for different fillers revealed evidence of microstructural changes, as shown in Figure 7. After subsequent PWHT, tempered martensite with $M_{23}C_6$ and MX precipitates that beautify the PAGBs and lath packet boundaries were noticed for both the filler in the weld fusion zone and the HAZs microstructure. Due to the higher availability of chromium (Cr) along the boundaries and the higher diffusion coefficient of carbon (C), the Cr-rich $M_{23}C_6$ -type precipitates formed preferentially along the PAGBs. The typical microstructure of the weld fusion zone having tempered lath martensitic microstructure for the E911 filler condition is shown in Figure 7(a). It was characterized by PAGBs, lath boundaries, tempered lath martensite, $M_{23}C_6$ -type precipitates, and fine MX-type precipitates. The secondary electron micrograph of FGHAZ is shown in Figure 7(b), which clearly reveals the presence of

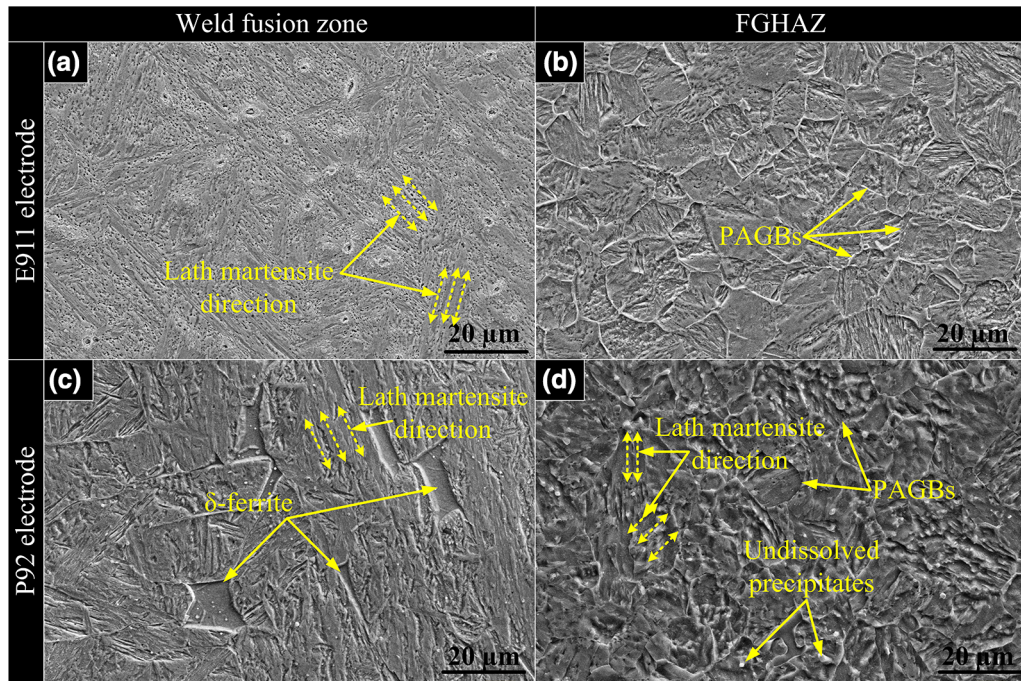


Fig. 6—Secondary electron micrograph in as-welded condition (a) weld fusion zone for E911 filler, (b) FGHAZ for E911 filler, (c) weld fusion zone for P92 filler, and (d) FGHAZ for P92 filler.

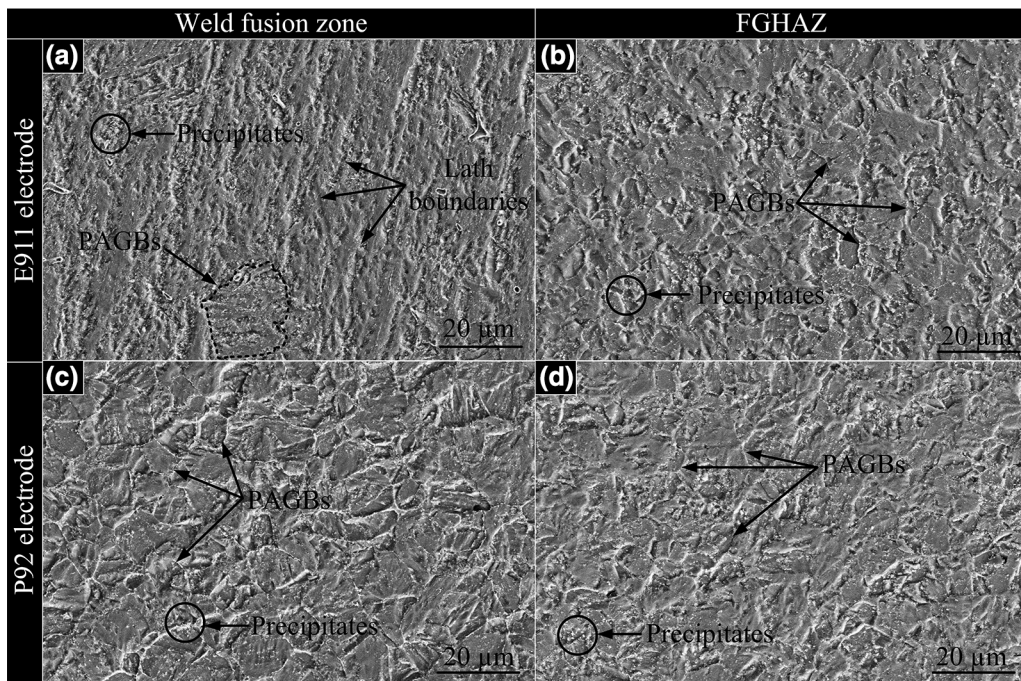


Fig. 7—Secondary electron micrograph in PWHT condition (a) weld fusion zone for E911 filler, (b) FGHAZ for E911 filler, (c) weld fusion zone for P92 filler, and (d) FGHAZ for P92 filler.

PAGBs, $M_{23}C_6$, and MX precipitate.^[46] In weld fusion zone of E911 filler, the columnar lath morphology is still observed after the PWHT while in the P92 filler, PWHT results in the transformation of laths from columnar to equiaxed morphology, as shown in Figure 7(c). In

FGHAZ, equiaxed tempered lath is formed for both the fillers, as shown in Figures 7(b) and (d).

A schematic of carbide evolution based on as-received, welding using filler and PWHT conditions is presented in Figure 8(a).^[47] In the as-received condition,

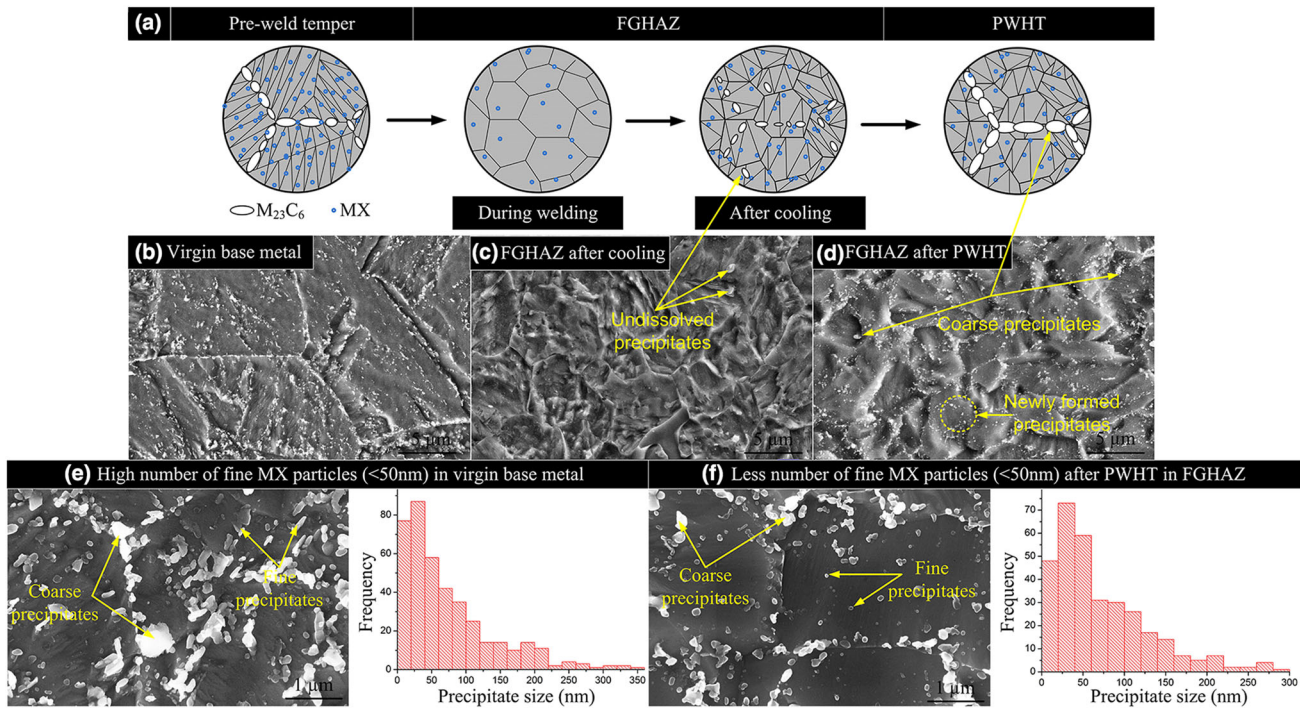


Fig. 8—(a) Schematic showing microstructure evolutions after welding and PWHT, (b), (c), (d) micrographs of base metal, FGHAZ after welding, FGHAZ after PWHT, respectively, (e) fine MX particles in base material, and (f) fine MX particles in FGHAZ after PWHT.

$M_{23}C_6$ is located along the PAGBs, packet boundaries, and martensite block, and $M_{23}C_6$ is in a near-equilibrium condition, as shown in Figure 8(b). In the as-received condition, the distribution of the precipitates and their morphology is shown in Figure 8(e). To prevent movement of boundaries, it is important to have $M_{23}C_6$ -type precipitates on the grain boundaries because $M_{23}C_6$ resulted in four times more pinning pressure than MX-type precipitates. Inside the martensite blocks and at the martensite block boundaries, MX-type precipitates are also present. After welding, some coarse $M_{23}C_6$ precipitates were noticed, but the MX remains unchanged due to the higher thermal stability, as shown in Figure 8(c) and also confirmed from the schematic diagram of the FGHAZ in the as-welded state. After PWHT, supersaturated carbon in the martensite matrix of the FGHAZ will support the growth of undissolved $M_{23}C_6$ instead of the formation of new $M_{23}C_6$ precipitates. For the same reason, the amount of newly formed MX precipitates will be less as compared to the as-received material condition, as shown in Figure 8(d) through (f).

The secondary electron micrographs showing the precipitate evolution in the FGHAZ after PWHT for E911 and P92 filler are given in Figure 9(a) and (b), respectively. The precipitate size present at PAGBs in FGHAZ was measured using Image J software as 107 ± 36 and 115 ± 32 nm for E911 and P92 filler, respectively. The size of precipitates present in the matrix region was measured to be 60 ± 16 and 62 ± 12 nm for E911 and P92 filler, respectively. For both the fillers, a negligible change was observed in the

size of precipitates present at PAGBs and in the matrix area, as shown in Figure 9(c). Some precipitates having size less than 40 nm were also seen in higher magnification micrograph that is confirmed as fine MX precipitates.^[48]

D. Tensile Test

For the transverse tensile test, fractured and un-fractured specimens for the as-welded and PWHT condition are shown in Figure 10. For each results, the averages of three tests are reported. In as-welded condition, for P92 filler, fracture occurred form FGHAZ, as shown in Figure 10(a). For E911 filler, fracture occurs in the ICHAZ, as shown in Figure 10(a). The FGHAZ and ICHAZ are considered as the softest zone in P92 weldments which is also confirmed form the hardness variation, as shown in Figure 14. After the PWHT, the fracture location was shifted from FGHAZ/ICHAZ to the over-tempered base metal for all specimens welded with E911 and P92 fillers, as shown in Figure 10(b). In as-welded condition, the un-fractured and fractured longitudinal tensile specimens for E911 and P92 fillers are shown in Figure 11.

Engineering stress–strain curve for longitudinal tensile tested specimens is shown in Figure 12(a). To find out the effect of different fillers on the tensile behavior of P92 steel weldments, the engineering and true stress–strain curves were imposed in as-welded condition, as shown in Figure 12(b). For both filler welds, the true stress–strain curve was noticed on top of engineering stress–strain curve. The true and engineering

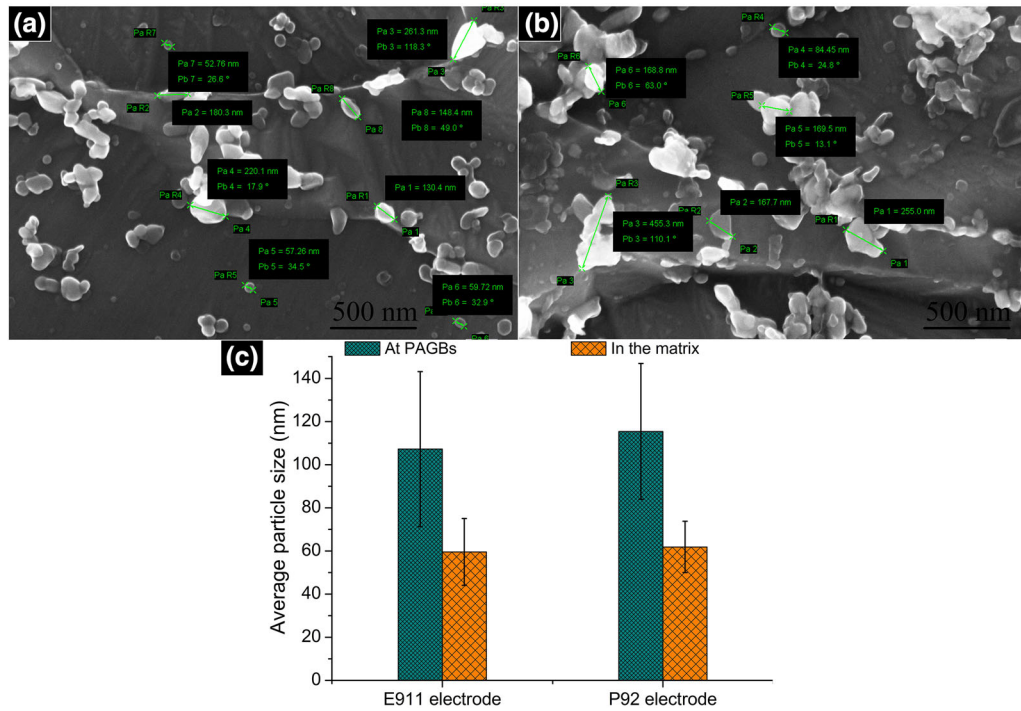


Fig. 9—Secondary electron micrograph of FGHAZ after PWHT (a) for E911 filler, (b) for P92 filler, and (c) average particle size in FGHAZ for different fillers.

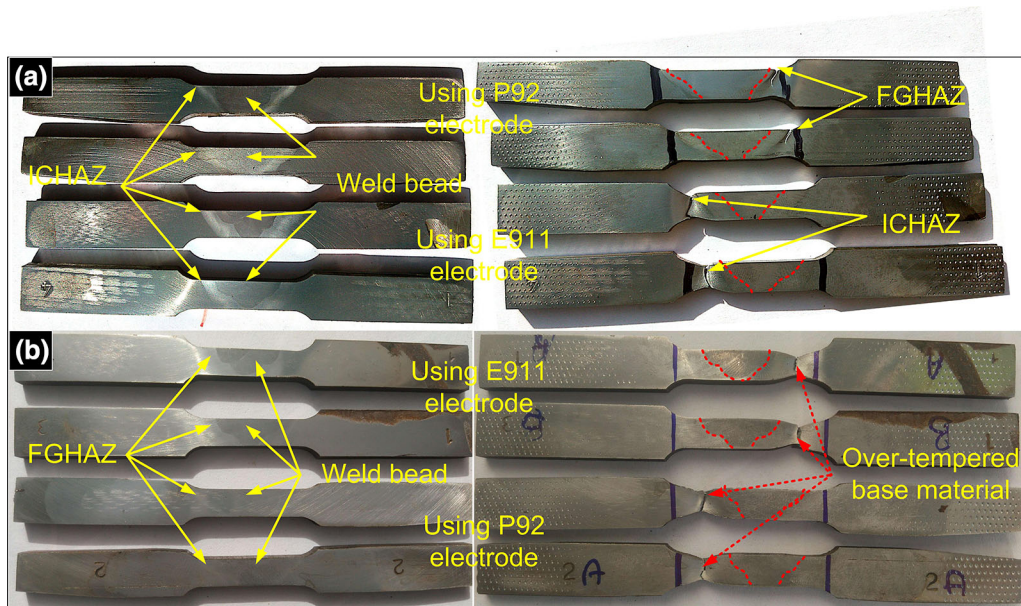


Fig. 10—Tensile specimens before and after the transverse tensile test in (a) as-welded condition and (b) PWHT condition.

stress–strain curves were shifted towards the higher side for P92 steel specimens welded with P92 filler. In as-welded condition, the ultimate tensile strength (UTS) of weld fusion zones of P92 steel weldments was measured to be 958 ± 35 and 1359 ± 38 using E911 and P92 filler, respectively. The percent elongations of the weld fusion zone were measured as 20 and 25 pct for

E911 and P92 filler, respectively. In the P92 filler, the higher strength of the weld was attributed to the higher weight percentage of carbon in the solution matrix as compared to E911 filler (Table I). The higher weight percentages of W and Mo in the P92 weld fusion zone also lead to the higher strength of the P92 filler weld as compared to the E911 filler weld. The higher weight

percentage of C, Mo, and W in the weld fusion zone of the P92 filler results in higher solid solution hardening that leads to higher strength. The engineering stress–strain curve for transverse tensile tested specimens welded with E911 and P92 fillers is shown in

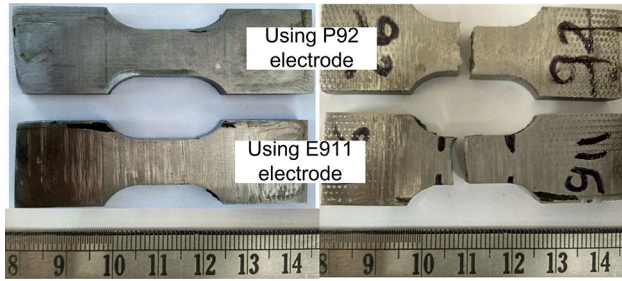
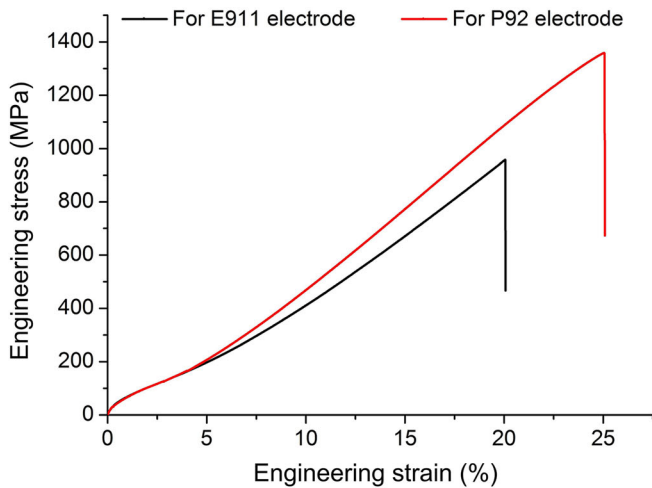


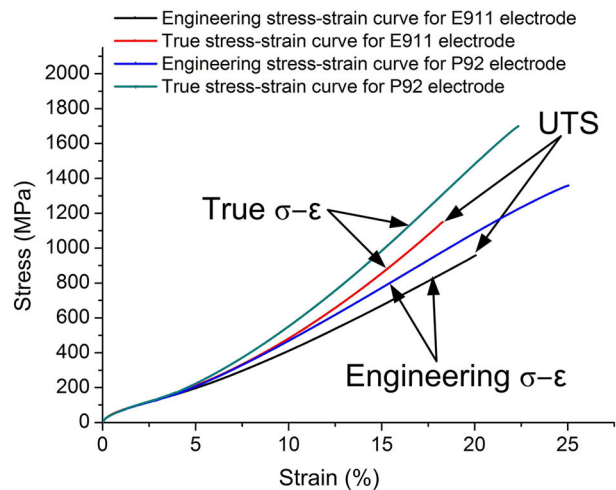
Fig. 11—Specimens before and after the longitudinal tensile test in as-welded condition.

Figure 12(c). In the transverse tensile tested specimens, serrations were also observed in the as-welded and PWHT conditions for both fillers. At a low strain rate, serrations are characterized as the repeated appearance of discontinuities in the stress–strain curve of deforming alloy. The engineering stress–strain curves were shifted towards the higher side for P92 steel filler weld specimens. After PWHT, the engineering stress–strain curves were also shifted towards the higher side for both filler weld specimens, as shown in Figure 12(c).

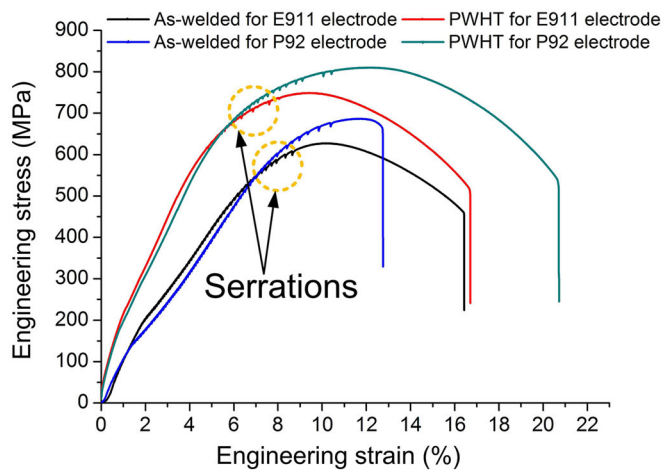
The UTS variation of the P92 steel weldments for different filler and post-weld conditions is given in Figure 13(a). In the as-welded condition, the UTS was measured to be 644 ± 24 and 674 ± 18 MPa for E911 and P92 filler, respectively. The value of UTS for the transverse welded joints was closer to the value of the as-received material UTS. In the transverse tensile tested specimen, fracture also occurred in the softest FGAZ and ICHAZ zone. The higher strength of weld for both E911 and P92 filler results in fracture from the softest



(a)



(b)



(c)

Fig. 12—(a) Longitudinal engineering stress–strain curve for different fillers, (b) true and engineering stress–strain curve in longitudinal samples with different fillers, and (c) transverse engineering stress–strain curve for different fillers and post-weld conditions.

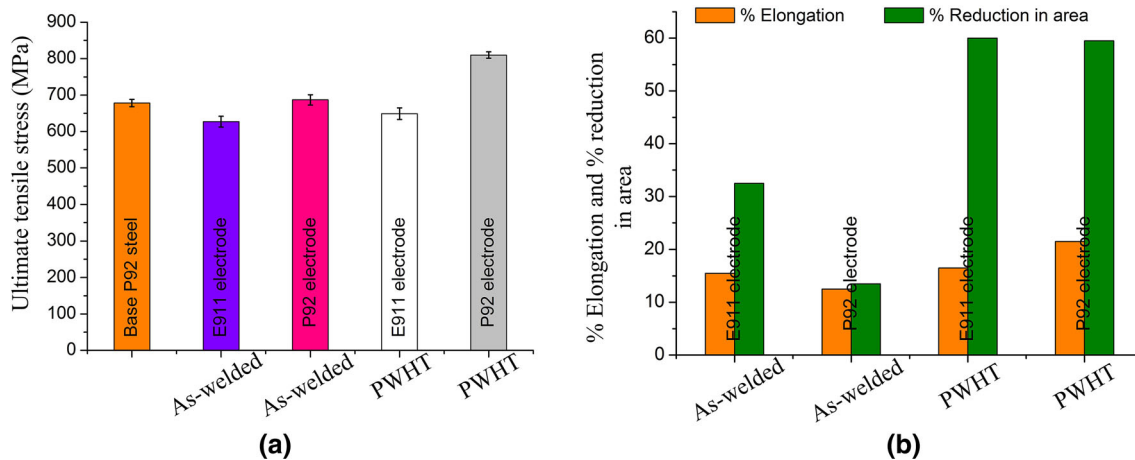


Fig. 13—For different fillers and post-weld conditions: (a) ultimate tensile strength and (b) percent elongation and percent reduction in area.

zone. After PWHT, the UTS was measured as 760 ± 16 and 786 ± 25 MPa for E911 and P92 filler, respectively, which is much higher than the as-received P92 steel UTS. The increase in strength might be due to precipitation of $M_{23}C_6$ and MX precipitates, which leads to precipitation hardening. In the as-welded condition, the percent elongation for transverse welded joints using E911 and P92 fillers was measured as 16 ± 3 and 12.5 ± 2.5 pct, respectively. The welded specimens have much lower values of percent elongation compared to as-received P92 steel (23 ± 2 pct). The low value of percent elongation in as-welded condition is attributed to formation of untempered lath martensite in weld fusion zone. After PWHT, the percent elongation remains same for E911 filler welds but it was observed to be increased for P92 filler, *i.e.*, from 12.5 ± 2.5 to 21 ± 4 pct. In as-welded state, the percent reduction in area was noticed to be much high in case of E911 filler welds as compared to P92 filler welds, as shown in Figure 13(b). The percent reduction in area was found to be increased after PWHT for both the filler, as shown in Figure 13(b).

E. Hardness

The hardness of P92 steel weldments depends on the presence of C and N in the solid solution matrix, the precipitates density, the presence of fine precipitates of MX (M: V, Nb; X: C, N) and the grain size.^[49,50] The variation in hardness for different filler and post-weld conditions of P92 steel welds is shown in Figure 14. In the as-welded condition, the average hardness of the weld fusion zone was measured to be 451 ± 20 and 571 ± 24 HV for the E911 and P92 fillers, respectively. The higher weight percentage of C in the weld fusion zone of P92 filler leads to solid solution hardening, which results in a higher average hardness in the P92 weld fusion zone for P92 filler as compared to E911 filler. The hardness was observed to decrease with distance from the weld fusion zone. The minimum hardness was measured in the soft ICHAZ zone. The

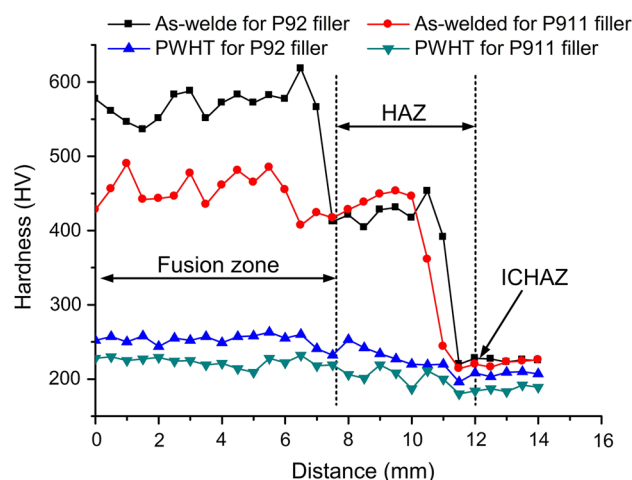


Fig. 14—Hardness variation for different filler and post-weld conditions from center of the weld fusion zone to the base material.

ICHAZ hardness was measured to be 214 and 220 HV for E911 and P92 filler, respectively. After PWHT, the average hardness of weld fusion zone was measured to be 224 ± 7 and 252 ± 8 HV for E911 and P92 fillers, respectively. The lowering in hardness of P92 weldments after the PWHT is attributed to the tempering of martensite and evolution of new fine MX and coarse $M_{23}C_6$ precipitates. However, PWHT did not affect so much to the hardness value of ICHAZ and the minimum hardness was still measured in soft ICHAZ zone. After the PWHT, the hardness of soft ICHAZ zone was measured to be 196 HV and 180 HV for P92 and E911 filler, respectively.

F. Charpy Toughness

To evaluate the HAZ impact toughness of the P92 weldments, notches were created in the samples. It was difficult to make notches exactly in the CGHAZ and ICHAZ because of the small width of the zones.

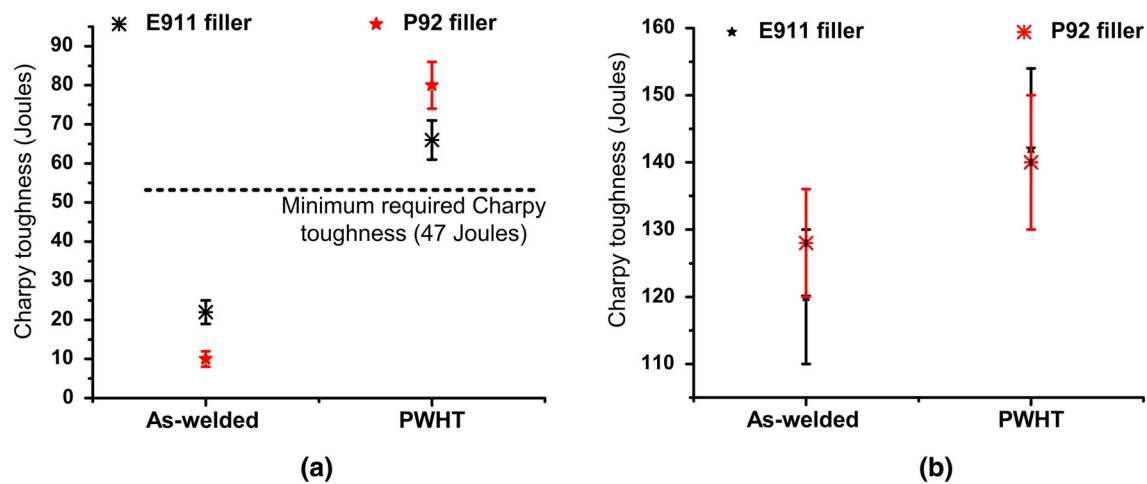


Fig. 15—Charpy toughness of (a) weld fusion zone and (b) HAZ for different fillers in as-welded and PWHT condition.

Notches were prepared adjacent to the weld fusion zone boundaries. Variation in the Charpy toughness of the weld fusion zone with respect to different filler and post-weld conditions is depicted in Figure 15(a). Three specimens were used to estimate the average impact energy of the weld fusion zone. It was noticed that the welds with P92 filler exhibited poor Charpy toughness in the weld fusion zone as compared to E911 filler welds. In the as-welded condition, poor Charpy toughness is attributed to untempered lath martensite. P92 steel welds require a minimum of 47 J during the hydro testing of vessels as per the EN1557:1997 specification. In the P92 filler weld fusion zone, there is higher V and Nb content (V-0.23 pct and Nb-0.06 pct) than in the E911 filler weld fusion zone (V-0.08 pct and Nb-0.05 pct). In P92 filler, the higher content of V and Nb in the weld fusion zone is responsible for the poor Charpy toughness value of the zone.^[51] The other fact that affects the Charpy toughness value is the higher weight percentage of C in the P92 filler weld fusion zone, which leads to the formation of brittle untempered martensite. In the as-welded condition, the Charpy toughness of the weld fusion zone for both P92 and E911 filler does not meet the minimum required Charpy toughness value of 47 Joules. After the PWHT, the Charpy toughness of the weld fusion zone was measured to be 66 ± 5 and 80 ± 6 J for E911 and P92 filler, as shown in Figure 15(a).

This represents the presence of secondary cracks in the crack initiation zone and a river-like pattern in the final fracture zone. The river-like pattern is formed when the cleavage fracture is forced to re-initiate at the boundary of a grain in a different orientation. The detailed view of the crack initiation zone was characterized by the quasi-cleavage facets and ductile tear ridges, as shown in Figure 17(c). In the as-welded condition, the top view of the fracture surface for E911 filler after the static tensile test is presented in Figure 17(d). The primary and secondary cracks appeared in the top view fracture surface. The detailed view of the final fracture zone was characterized by the

ductile tear ridges, quasi-cleavage facets and transgranular ductile dimples shown in Figure 17(e). The percentage area of ductile dimples for E911 filler was higher than the fracture surface for the P92 filler.

G. Fracture Surface Morphology

Figure 16(a) through (b) represents the final fracture zones of the longitudinal tensile tested specimen for E911 and P92 fillers, respectively. The fracture surface was characterized with the quasi-cleavage facets and ductile dimples for specimens welded with E911 filler and P92, as shown in Figure 16(a) through (b). However, in P92 filler percentage area of cleavage facets was observed to be much higher than E911 filler. In case of P92 filler, fewer amount of ductile dimples were observed besides the area of cleavage facets. In as-welded condition, the crack initiation zone and final fracture zone of across the weld tensile tested specimens for P92 filler were represented in Figure 17(a) and (c), respectively. The detailed view of final fracture zone was characterized by mixed mode of the fracture. Both ductile dimples and cleavage facets are observed at the fracture surface, as shown in Figure 17(a). However, the area of cleavage facets is observed to be higher than ductile dimples. Microvoid coalescence is the mechanism of ductile transgranular fracture and cleavage is the mechanism of brittle transgranular fracture which occurs through cleaving of the crystals along crystallographic planes.^[52] The top view of fracture surface for as-welded P92 steel using P92 filler in across the weld direction after the tensile test is shown in Figure 17(b). It represents the presence of secondary cracks in the crack initiation zone and river-like pattern in the final fracture zone. The river-like pattern is formed when the cleavage fracture is forced to re-initiate at the boundary of a grain in a different orientation. The detailed view of crack initiation zone was characterized by the quasi-cleavage facets and ductile tear ridges, as shown in Figure 17(c). In as-welded condition, the top view of fracture surface for E911 filler after the static tensile test

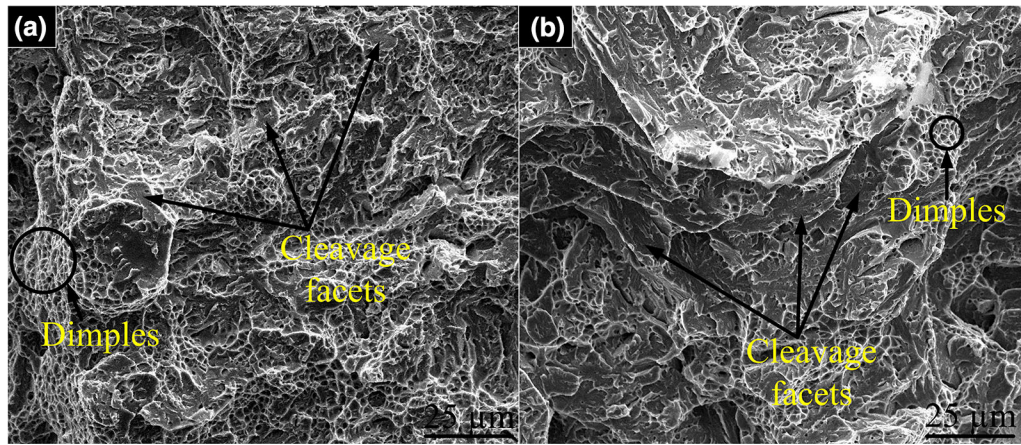


Fig. 16—Fracture surface morphology of longitudinal tensile specimen (a) using E911 filler and (b) using P92 filler.

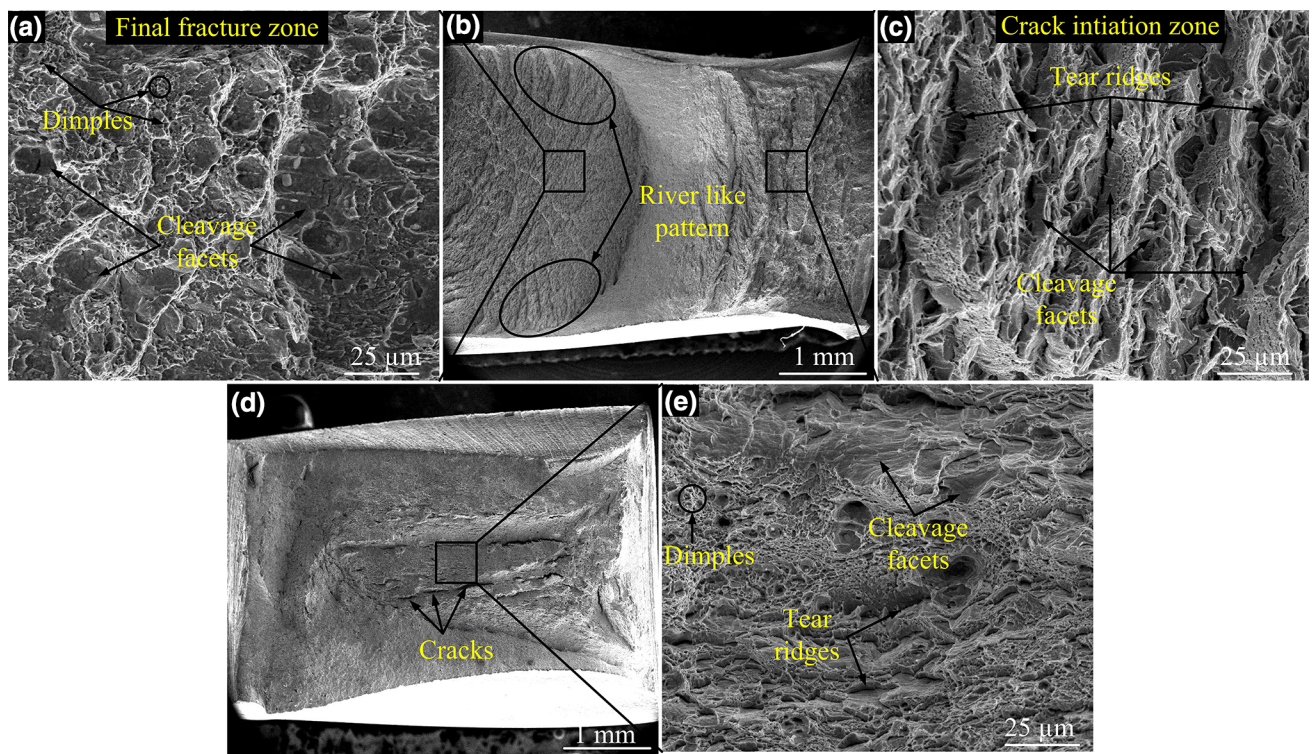


Fig. 17—Fracture surface appearance across the welded specimen in as-welded condition (a), (b) and (c) using P92 filler and (d) and (e) using E911 filler.

is represented in Figure 17(d). The primary and secondary cracks appeared in the top view fracture surface. The detailed view of final fracture zone was characterized by the ductile tear ridges, quasi-cleavage facets and transgranular ductile dimples as shown in Figure 17(e). The percentage area of ductile dimples for E911 filler was higher than the fracture surface for the P92 filler.

After the PWHT, the top view of fracture surfaces for welded using E911 and P92 filler was shown in Figure 18(a) and (c), respectively. After PWHT, the

numbers of primary and secondary cracks were decreased as shown in Figure 18(a). The detailed view of final fracture zone for E911 filler was characterized by mainly ductile dimples and quasi-cleavage facets as shown in Figure 18(b). The percentage area of ductile dimples was enhanced after PWHT for E911 filler. After PWHT, the river-like pattern and number of cracks were decreased as compared to as-welded condition for the P92 filler as shown in Figure 18(c). The width of tear ridges and percentage area of cleavage facets were decreased after PWHT in the final fracture zone for the P92 filler as

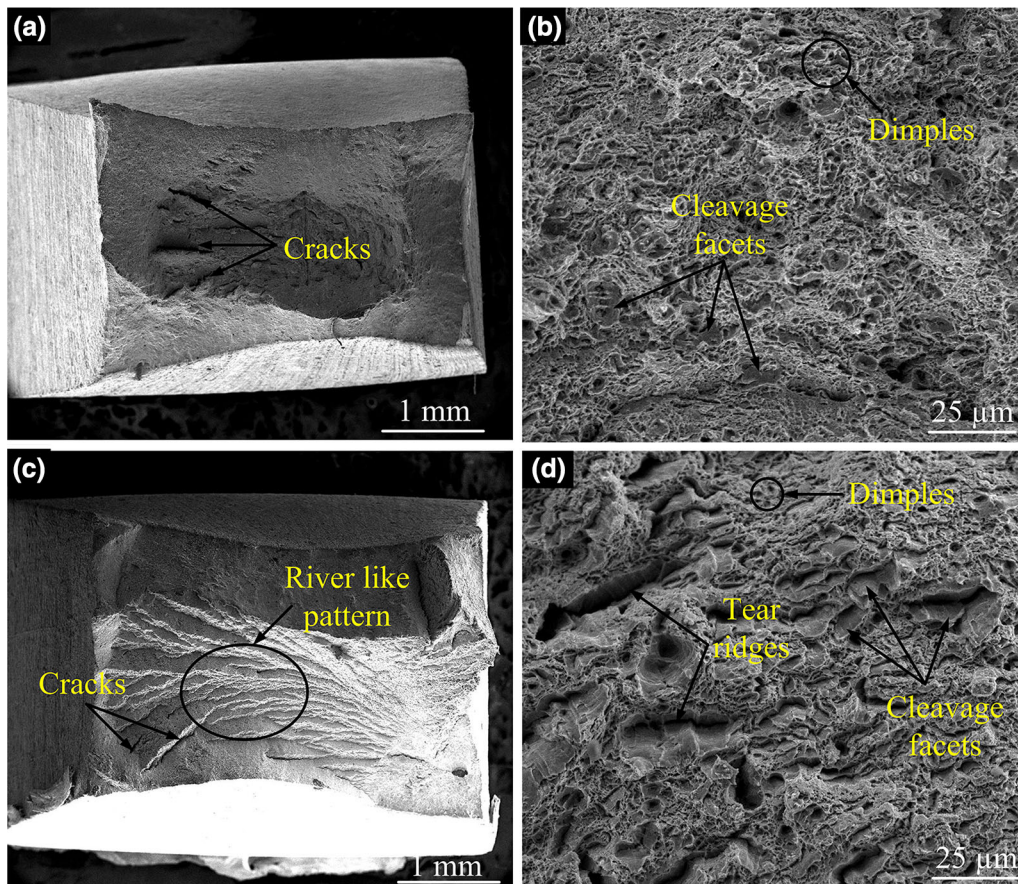


Fig. 18—Fracture surface appearance across the welded specimen after PWHT (a) and (b) using E911 filler and (c) and (d) using P92 filler.

shown in Figure 18(d). After PWHT, the percentage area of ductile dimples was also increased for the P92 filler.

IV. CONCLUSIONS

- P92 steel weldments were prepared successfully using P92 and E911 filler.
- In the as-welded condition, the ultimate tensile strength (UTS) of the P92 steel weldment for E911 filler was measured to be 958 ± 35 and 644 ± 24 for longitudinal and transverse tensile tested specimens, respectively. The UTS of P92 filler welds was measured to be 1359 ± 38 and 674 ± 18 from longitudinal and transverse tensile tests, respectively. The higher strength in the P92 filler was attributed to the higher weight percentage of W and Mo in the P92 weld fusion zone as compared to E911 filler welds. After the PWHT, the ultimate tensile strength was found to be increased in the transverse direction of the weld, whereas the value decreased in the longitudinal direction for both the fillers.
- In the as-welded condition, transverse tensile specimens were fractured from the fine-grained heat-affected zone or inter-critical heat-affected zone (FGHAZ/ICHAZ), but after PWHT the fracture location was shifted to over-tempered base metal from the FGHAZ/ICHAZ.
- After PWHT, a considerable lowering in hardness was observed throughout the weldments. The average hardness of the weld fusion zone was effectively decreased to 224 ± 7 and 252 ± 8 HV from 451 ± 20 and 571 ± 24 HV for the E911 and P92 fillers, respectively.
- In the as-welded condition, the weld fusion zone shows the poor Charpy toughness of the P92 steel welds for both the fillers. In the as-welded condition, poor Charpy toughness was measured for the P92 filler due to the higher weight percentage of V and Nb in the weld fusion zone. In the as-welded condition, the Charpy toughness was measured to be lower than the minimum required Charpy toughness value for both fillers. After PWHT, the weld fusion zone Charpy toughness of the P92 steel welds was measured as 66 ± 5 and 80 ± 6 J for the E911 and P92 fillers, respectively, which was higher than the minimum required Charpy toughness value.
- The Charpy toughness of HAZs in the as-welded condition was measured as 120 ± 7 and 128 ± 8 J for the E911 and P92 fillers, respectively.

- The HAZ Charpy toughness of P92 steel welds after PWHT was measured as 142 ± 8 and 140 ± 5 J for the E911 and P92 fillers, respectively.

REFERENCES

1. N. Saini, C. Pandey, and M.M. Mahapatra: *J. Mater. Eng. Perform.*, 2017, vol. 26, pp. 5414–24.
2. C. Pandey, M.M. Mahapatra, P. Kumar, and N. Saini: *J. Nucl. Mater.*, 2018, vol. 498, pp. 176–86.
3. A. Zieliński: *J. Achiev. Mater. Manuf. Eng.*, 2012, vol. 54, pp. 67–74.
4. A. Marek and J. Okrajni: *J. Mater. Eng. Perform.*, 2014, vol. 23, pp. 31–8.
5. N. Saini, C. Pandey, and M.M. Mahapatra: *Int. J. Hydrog. Energy*, 2017, pp. 1–11.
6. N. Saini, C. Pandey, M.M. Mahapatra, H.K. Narang, R.S. Mulik, and P. Kumar: *Eng. Fail. Anal.*, 2017, pp. 1–9.
7. N. Saini, C. Pandey, M.M. Mahapatra, and R.S. Mulik: *Mater. Sci. Eng. A*, 2018, vol. 711, pp. 37–43.
8. C.D. Lundin: *Mater. Des.*, 1991, vol. 12, pp. 193–97.
9. C. Pandey, M.M. Mahapatra, P. Kumar, and N. Saini: *J. Alloys Compd.*, 2018, vol. 743, pp. 332–64.
10. J. Lecomte-Beckers, M. Carton, F. Schubert, and P.J. Ennis: *Proceedings of the 8th Liege Conference Part I*, 2006, vol. 53, pp. 1–631.
11. T. Sakthivel, M. Vasudevan, K. Laha, P. Parameswaran, K.S. Chandravathi, S. Panneer Selvi, V. Maduraimuthu, and M.D. Mathew: *Mater. Sci. Eng. A*, 2014, vol. 591, pp. 111–20.
12. R. Viswanathan, J. Sarver, and J.M. Tanzosh: *J. Mater. Eng. Perform.*, 2006, vol. 15, pp. 255–74.
13. T. Sakthivel, K. Laha, P. Parameswaran, S. Panneer Selvi, K.S. Chandravathi, and M.D. Mathew: *Trans. Indian Inst. Met.*, 2015, vol. 68, pp. 411–21.
14. K. Maruyama, K. Sawada, and J. Koike: *ISIJ Int.*, 2001, vol. 41, pp. 641–53.
15. N. Saini, C. Pandey, and M.M. Mahapatra: *Mater. Sci. Eng. A*, 2017, vol. 688, pp. 250–61.
16. E. Sambamurthy, S. Dutta, A.K. Panda, A. Mitra, and R.K. Roy: *Int. J. Press. Vessel. Pip.*, 2014, vols. 123–124, pp. 86–91.
17. V. Sklenicka, K. Kucharova, M. Svobodová, M. Kvapilová, P. Král, and L. Horváth: *Mater. Charact.*, 2016, vol. 119, pp. 1–12.
18. M. Debicki, A.W. Marshall, Z. Zhang, G.B. Holloway, and H. Lane: in *Welding and repair technology for power plants-5th International EPRI RRAC Conference*, 2002, pp. 1–13.
19. C. Chovet, E. Galand, and B. Leduey: *Weld. World*, 2008, vol. 52, pp. 18–26.
20. R. Bruscati: *Weld. Res. Suppl.*, 1970, pp. 148–56.
21. C. Pandey, A. Giri, M.M. Mahapatra, and P. Kumar: *Met. Mater. Int.*, 2017, vol. 23, pp. 148–62.
22. S.T. Mandziej, A. Výrostková, and C. Chovet: *Weld. World*, 2011, vol. 55, pp. 37–51.
23. L. Falat, J. Kepic, L. Ciripova, P. Sevc, and I. Dlouhy: *J. Mater. Res.*, 2016, vol. 31, pp. 1532–43.
24. J. Onoro: *Int. J. Press. Vessel. Pip.*, 2006, vol. 83, pp. 540–45.
25. C. Pandey, M.M. Mahapatra, P. Kumar, N. Saini, J.G. Thakre, R.S. Vidyarthi, and H.K. Narang: *Archiv. Civ. Mech. Eng.*, 2018, vol. 18, pp. 713–22.
26. C. Pandey, M.M. Mahapatra, P. Kumar, and N. Saini: *Mater. Sci. Eng. A*, 2018, vol. 712, pp. 720–37.
27. K.M. Chalk, P.H. Shipway, and D.J. Allen: *Sci. Technol. Weld. Join.*, 2011, vol. 16, pp. 613–8.
28. W. Xue, Q.G. Pan, Y.Y. Ren, W. Shang, H.Q. Zeng, and H. Liu: *Mater. Sci. Eng. A*, 2012, vol. 552, pp. 493–501.
29. C. Pandey, M.M. Mahapatra, P. Kumar, and N. Saini: *Mater. Sci. Eng. A*, 2018, vol. 710, pp. 86–101.
30. H. Cerjak and E. Letofsky: *Sci. Technol. Weld. Join.*, 1996, vol. 1, pp. 36–42.
31. M.R. Dodo, T. Ause, M.A. Adamu, and Y.M. Ibrahim: *Niger. J. Tech.*, 2016, vol. 35, pp. 337–43.
32. N. Saini, C. Pandey, and M.M. Mahapatra: *Trans. Indian Inst. Met.*, DOI: 10.1007/s12666-017-1145-3.
33. C. Pandey and M.M. Mahapatra: *J. Mater. Eng. Perform.*, 2016, vol. 25, pp. 2195–2210.
34. ASTM E8/E8M-16a, ASTM International, West Conshohocken, PA, 2016.
35. AWS B4.0, American Welding Society, 2016.
36. C.G. Panait, A. Zielinska-Lipiec, T. Koziel, A. Czyska-filemonowicz, A.F. Gourgues-Lorenzon, and W. Bendick: *Mater. Sci. Eng. A*, 2010, vol. 527, pp. 4062–69.
37. C. Pandey, M.M. Mahapatra, P. Kumar, and N. Saini: *Mater. Sci. Eng. A*, 2017, vol. 685, pp. 39–49.
38. D.R. Barbadikar, G.S. Deshmukh, L. Maddi, K. Laha, P. Parameswaran, A.R. Ballal, D.R. Peshwe, R.K. Paretkar, M. Nandagopal, and M.D. Mathew: *Int. J. Press. Vessel. Pip.*, 2015, vols. 132–133, pp. 97–105.
39. C. Pandey, A. Giri, and M.M. Mahapatra: *Mater. Sci. Eng. A*, 2016, vol. 657, pp. 173–84.
40. T. Shrestha, S.F. Alsaagabi, I. Charit, G.P. Potirniche, M.V. Glazoff, and H.F. Lopez: *Metals*, 2015, vol. 5, pp. 131–49.
41. Z. Zhang, G. Holloway, and A. Marshall: *Weld. World*, 2008, vol. 6, pp. 1–13.
42. B. Silwal, L. Li, A. Deceuster, and B. Griffiths: *Weld. Res.*, 2013, vol. 92, pp. 80s–87s.
43. J. Cao, Y. Gong, K. Zhu, Z.G. Yang, X.M. Luo, and F.M. Gu: *Mater. Des.*, 2011, vol. 32, pp. 2763–70.
44. L. Milovic, T. Vuherer, M. Vrhovac, and M. Stankovic: *Mater. Des.* 2013, vol. 46, pp. 660–7.
45. C. Pandey, M.M. Mahapatra, P. Kumar, and N. Saini: *J. Manuf. Process.*, 2018, vol. 31, pp. 247–59.
46. S.S. Wang, D.L. Peng, L. Chang, and X.D. Hui: *Mater. Des.*, 2013, vol. 50, pp. 174–80.
47. C. Pandey, M.M. Mahapatra, P. Kumar, and N. Saini: *Mater. Sci. Eng. A*, 2018, vol. 710, pp. 86–101.
48. C.G. Panait, W. Bendick, A. Fuchsmann, A.F. Gourgues-Lorenzon, and J. Besson: *Int. J. Press. Vessel. Pip.*, 2010, vol. 87, pp. 326–35.
49. C. Pandey and M.M. Mahapatra: *Trans. Indian Inst. Met.*, 2016, vol. 69, pp. 1657–73.
50. C. Pandey, M.M. Mahapatra, P. Kumar, N. Saini, and J.G. Thakre: *Trans. Indian Inst. Met.* DOI: 10.1007/s12666-017-1215-6.
51. B. Arivazhagan and M. Vasudevan: *J. Manuf. Process.*, 2014, vol. 16, pp. 305–11.
52. C. Pandey, N. Saini, M.M. Mahapatra, and P. Kumar: *Eng. Fail. Anal.*, 2016, vol. 71, pp. 131–47.